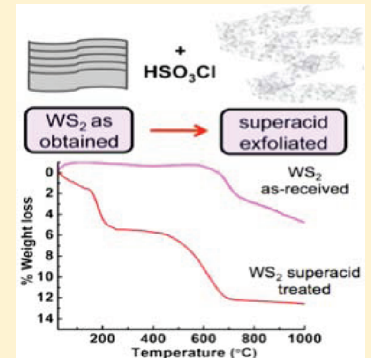


Synthesis of Surface-Functionalized WS₂ Nanosheets and Performance as Li-Ion Battery Anodes

R. Bhandavat, L. David, and G. Singh*

Department of Mechanical and Nuclear Engineering, Kansas State University, Manhattan, Kansas 66506, United States

ABSTRACT: Separation of bulk tungsten disulfide (or WS₂) into few-layer two-dimensional (2-D) crystals is of interest because of their high surface area for certain chemical processes and size-dependent optical and electronic characteristics. Herein, we demonstrate a process that involves the physical separation of weakly bonded WS₂ layers by use of a strong acid treatment (chlorosulfonic acid) at 2 mg/mL, followed by quenching in deionized (DI) water. X-ray photoelectron spectroscopy of the superacid-treated WS₂ suggests the formation of W–O type bonds, signifying oxidation of tungsten and reduction of the sulfur phase. Thermogravimetric analysis showed a three-phase weight-loss pattern, suggesting acid functionalization of WS₂ surfaces. We also studied the electrochemical behavior of an acid-treated WS₂ anode in a lithium half-cell configuration that showed a three-step charge–discharge behavior, characteristic of a conversion reaction. The electrochemical capacity was 118 mAh/g after 50 cycles.



SECTION: Energy Conversion and Storage; Energy and Charge Transport

Inorganic transition metal dichalcogenide (TMDC) materials (such as WS₂ and MoS₂) are of interest to the scientific community because of their unique layered structure and related functional properties that may find use in applications related to energy storage,¹ field effect transistors,² and nanocomposite coatings.³ TMDC structure comprises of covalent bonded two-dimensional (2-D) sandwiched units that are separated by weak van der Waals spacing. This spacing can be intercalated by guest species to form a variety of compounds useful for scientific applications such as rechargeable battery anodes and light-emitting diodes.^{4,5} A combination of constituent transition metal, chalcogen, or guest species can be selected to form a variety of intercalated compounds with desired architecture and functional properties.^{6,7}

Bulk WS₂ has been studied for many years as a high-temperature lubricant as well as an intercalation material in rechargeable batteries. However, it is only recently that the focus has shifted onto large-scale exfoliation of WS₂ (and other TMDCs) into single- or few-layer sheets for use in optoelectronic and electrochemical applications. Certain properties of TMDCs can only be realized in their 2-D crystals; for example, bulk MoS₂, which has an indirect band gap of 1.2 eV, becomes a direct band gap material (band gap ~1.8 eV) when exfoliated to single or few layers. Theoretical studies have shown that, under the influence of external electric fields (up to 3 V/nm), the band gap of semiconducting bilayered TMDCs such as WS₂ is tunable (0–1.5 eV).⁸ Moreover, in the case of Li-ion battery anodes, nanostructured TMDC is likely to allow increased Li-ion intercalation/deintercalation due to the high surface area and shorter diffusion path for Li-ion transport.

Various techniques involving synthesis of nanostructured WS₂ have been developed in the past decade or so. Feng et al.⁴

proposed a rheological phase reaction for synthesis of WS₂ nanoflakes, while Seo et al.⁹ utilized W₁₈O₄₉ nanorod sulfurization to obtain WS₂ nanosheet crystals. More recently, Wu et al.¹⁰ synthesized WS₂ nanosheets by ball-milling WO₃ and annealing it with sulfur at 500–800 °C. Matte et al.¹¹ demonstrated exfoliation of bulk WS₂ into single or few layers by intercalation with lithium in water; the reaction involved the formation of lithium hydroxide and evolution of hydrogen gas. Although small, single- or few-layered WS₂ sheets can be prepared, these methods are difficult to be scaled up for high volume production. A more attractive option is the chemical-mechanical exfoliation of WS₂ that could yield large quantities of atomically thin WS₂ sheets. Recently, Coleman et al. have shown that mechanical exfoliation of bulk WS₂ into few-layered sheets (10–15 layers) is possible by use of common organic solvents.¹²

Alternatively, methods for obtaining single- and few-layer graphene sheets in liquid solvents are now well documented.^{13–15} In particular, a study by Behabtu et al., involving the use of chlorosulfonic acid (ClSO₃H, superacid) for exfoliation of graphite into large-area graphene is of interest, as the exfoliation in superacid was observed to be almost instantaneous.¹⁶ It was suggested that the superacid could protonate carbon atoms, thereby inducing electrostatic repulsive forces larger than the van der Waals interatomic attraction forces, resulting in graphene-layer separation.^{16,17} Mainly composed of sulfuric and hydrochloric acid, superacid was demonstrated to be more effective than other acids, and its

Received: April 17, 2012

Accepted: May 18, 2012

Published: May 18, 2012

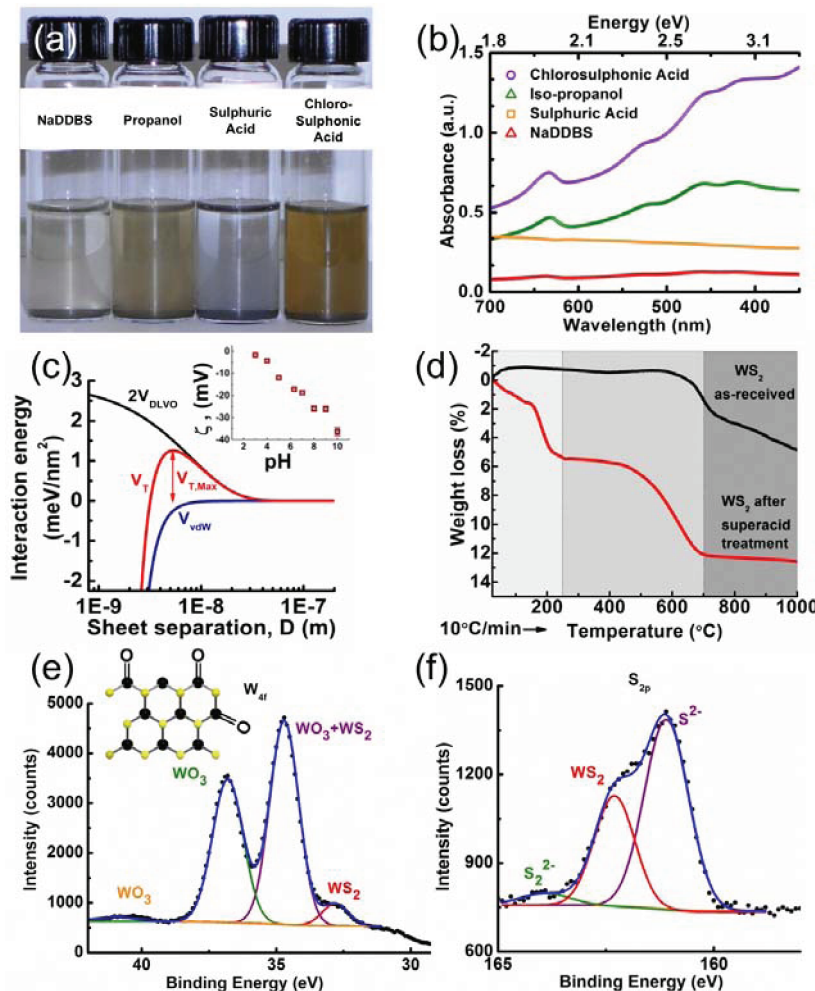


Figure 1. (a) Comparison of WS₂ dispersions in various solvents including superacid after keeping stable for 24 h. (WS₂ loading was held the same for all solvents at 2 mg/mL). (b) Comparative UV spectrum for various dispersions; the high UV absorbance intensity of superacid-treated WS₂ is highlighted. (c) Calculated total interaction potential energy (V_T), repulsion (V_{DLVO}), and attraction energy (V_{vdW}) (per unit area) with increasing WS₂ sheet separation distance (log scale) is shown. Inset: Experimentally measured zeta potential measurements, showing better dispersion stability at higher pH values. (d) Comparative TGA plot of the as-received and superacid-treated WS₂. (e) W_{4f} and (f) S_{2p} XPS spectra of the superacid-treated WS₂ (dots: measured data; line: curve fitted data).

concentration directly influenced graphene dispersion quality in the solution.¹⁸

On the basis of these promising results obtained for graphene, we studied superacid treatment of WS₂ with an overall aim to produce large-area, few-layer WS₂ sheets in large quantities. Since the surface energy of WS₂ sheets is relatively high, use of conventional methods involving liquid-phase exfoliation may not be very effective in forming stable/high-yield dispersions. More importantly, similar to graphene, the use of superacid may not significantly alter the WS₂ chemistry and may also reduce the mechanical force required for its exfoliation.

As far as applications are concerned, chemically modified WS₂ (or W–O–S type materials) based nanofibers, sheets, rolls, and nanotubes (all prepared by bottom-up fabrication approaches) have shown improved performance as Li-ion battery anodes.^{19–21} The earliest electrochemical study of pristine crystalline 3R-WS₂ powder was carried out by Julien et al., demonstrating up to 0.6 mols of Li-ions intercalating per mole of WS₂.^{22,23} In an independent work, Du et al.²⁴ showed that higher electrochemical performance of layered TMDCs can be achieved by increasing their surface (edges) area. Owing

to its novel architecture, the restacked WS₂ nanosheets could result in improved electrochemical performance and enhance our understanding of TMDC materials. The superacid treatment of WS₂ could result in increased sites for Li-ion intercalation, putting a check on first-cycle loss and thereby improving the reversible capacity. Hence, we analyzed the structure-performance relationship of superacid-exfoliated WS₂ and compared its electrochemical performance with that of bulk WS₂ from the literature.

Figure 1a shows the visual concentrations of the comparative dispersions after they were kept stable for 24 h. All dispersions except sulphuric acid showed greenish color, as typically expected for WS₂ dispersions. Visual inspection of WS₂ in superacid suggests a stable dispersion. Figure 1b shows the comparative absorption spectra of WS₂ sheets in various solvents, collected from only the top portion of the extracted dispersant and subtracting the background scattering. The intensity of optical absorbance peaks is considered a good measure of concentration of exfoliated sheets.²⁵ Hence, the higher absorbance intensity for the superacid dispersion (over the entire wavelength range) clearly implies higher molar concentration (density) of WS₂ absorbing species.

As we anticipate that superacid protonates the WS_2 surfaces, these charged surfaces can experience electrostatic repulsion forces and form a stable dispersion in aqueous solution (also observed visually). ζ potential measurements can quantify this surface charge existing on WS_2 sheet surfaces and hence help in establishing the dispersion stability. The ζ potential measured at varying solution pH with the same WS_2 concentration can provide an understanding of the pH-dependent WS_2 sheet stability in the solution. Hence, a separate solution of 1 mg/mL WS_2 in superacid (top portion) was used for ζ potential measurements. The surface potential showed a range varying from -1.67 mV at pH of 3 to -36.3 mV at pH of 10, shown as an insert in Figure 1c. As higher surface potential (negative) implies more stable suspensions, based on the obtained results, higher pH suggests a larger exposed WS_2 sheet surface.

For ζ potential measurements, the pH was varied by adding 0.01 M NaOH solution. Also, since the contribution from dissociated OH^- ions in the measured potential is minimal, it was neglected in the analysis. The lower pH range was limited to protect the instrument electrode. This dependence of surface potential on pH is similar to that observed for exfoliated (surface-functionalized) graphene sheets by Lotya et al.²⁵ Further, we used their model of graphene stabilization mechanism for explaining the superacid– WS_2 interaction mechanism.

Accordingly, the total potential energy (V_T) at the surface interaction of two adjacent WS_2 sheets is the difference in repulsive potential energy (V_{DLVO}) and attractive van der Waals energy (V_{vdW}). V_{DLVO} for WS_2 surfaces is determined using the measured ζ potential, surfactant concentration, and distance between two separated sheets, and V_{vdW} is calculated using atomic density and surface energy. The total potential energy is then given by $V_T \approx V_{\text{DLVO}} - V_{\text{vdW}} = 4A\epsilon_r\epsilon_0\kappa\zeta^2 e^{-\kappa D} - A\pi\rho^2 C/2D^4$, where A is the area of WS_2 sheet, ρ is the number of atoms per unit area, ϵ_r and ϵ_0 are the relative permittivity of water (80.1 at 20 °C) and the absolute permittivity (8.85×10^{-12} F/m), respectively, ζ is the experimentally measured surface potential (36.3 mV), D is the distance of sheet separation, $\rho^2 C$ is the estimated surface energy per unit area¹² (approximately 2.06×10^{-38} J/m²), and κ is the double-layer thickness given as $1/[\epsilon_r\epsilon_0 kT/2e^2 n_0]^{0.5}$ ($n_0 = 9.05 \times 10^{23}$ is the number of surfactant molecules per unit volume of solution; $e = 1.6 \times 10^{-19}$ C). Figure 1c is the plot for total interaction energy per unit area of the sheet (V_T/A).

As shown in Figure 1d, the as-received WS_2 was found to be thermally stable up to 600 °C in flowing air, but the acid-treated WS_2 showed a low-temperature weight loss probably due to the presence of water vapor and other volatile contaminants. Beyond 400 °C, the weight loss of superacid-treated WS_2 was more significant than pristine WS_2 , most likely due to the loss of acidic residues and separated sheets.²⁶ Also, in the temperature range of 400–500 °C, WS_2 tends to oxidize to form WO_3 in an exothermic process, which was observed as a major weight loss in both the specimens.²⁷ Additionally, beyond 700 °C, the superacid-treated WS_2 appeared more stable than pristine WS_2 , which showed a continuous weight loss.

The XPS analysis for the superacid-treated WS_2 specimen reveals mainly two states of tungsten evidenced by two distinct peaks at 34.7 and 36.8 eV (Figure 1e). While majority of tungsten disulfide remained in the pristine form (low energy peak), the presence of the W–O peak at 36.8 eV suggests partial oxidation of WS_2 as a result of acid treatment.

The scanning electron microscopy (SEM) and transmission electron microscopy (TEM) images before (Figure 2a,c)

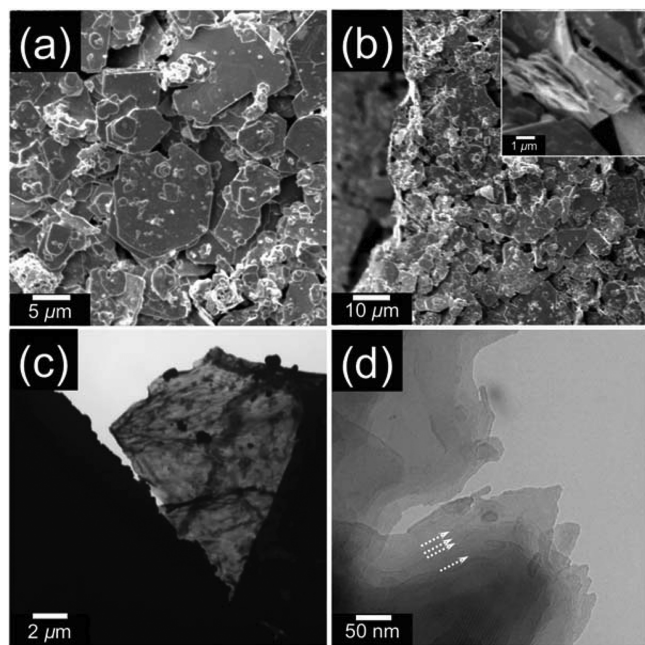


Figure 2. (a,c) SEM and TEM images of the as-obtained WS_2 crystal powder, respectively. (b,d) SEM and TEM images of superacid-treated WS_2 , respectively. Inset in panel b is the high-magnification SEM image, and arrows in panel d indicate individual WS_2 layers.

superacid treatment chiefly showed a distribution of multi-layered sheets, whereas after the superacid treatment, some instances of separated layered sheets were observed in SEM, and few-layer WS_2 flakes were apparently visible under the TEM (Figure 2b,d). The average size of the exfoliated sheets varied from approximately 3 to 5 μm .

Figure 3a shows the restacked WS_2 sheets laid on copper current collector, used as the anode for battery assembly. Under low resolution, the coating surface appeared very uniform, with an approximate particle size of 5–10 μm and the remaining space filled by soft-looking acetylene black. Formation of a solid–electrolyte interphase (SEI) layer over the restacked WS_2 sheets is visible with few cracks for the completely deintercalated anode (Figure 3b). The XPS spectra were also collected for the cycled anodes by dissembling the cell after 20 electrochemical cycles. The anode coating was gently cleaned with dimethyl carbonate to expose its surface for analysis. As shown in Figure 3c, the $\text{W}_{4\text{f}}$ valence energy band exhibited two major peaks, which were individually deconvoluted into doublets. The low-energy peak at 31.4 eV was assigned to reduced tungsten at 31.3 eV and the high-energy peak at 33.4 eV to both tungsten and unreacted tungsten disulfide. The second broad high-energy peak at 33.5 eV was attributed to native WS_2 .

The $\text{Li}_{1\text{s}}$ energy peak appeared less intense with the existence of free lithium, LiWO_4 , and Li_2SO_4 phases in the specimen.^{28,29} The $\text{S}_{2\text{p}}$ valence band indicated a broad peak at 161.1 eV, which was deconvoluted into one peak at 161.9 eV collectively associated with unreacted WS_2 and lithium intercalated WS_2 ,³⁰ while the peak at 163.1 eV is purely due to intercalated WS_2 .³⁰ Table 1 presents the summary of elemental composition of the anode surface at various stages.

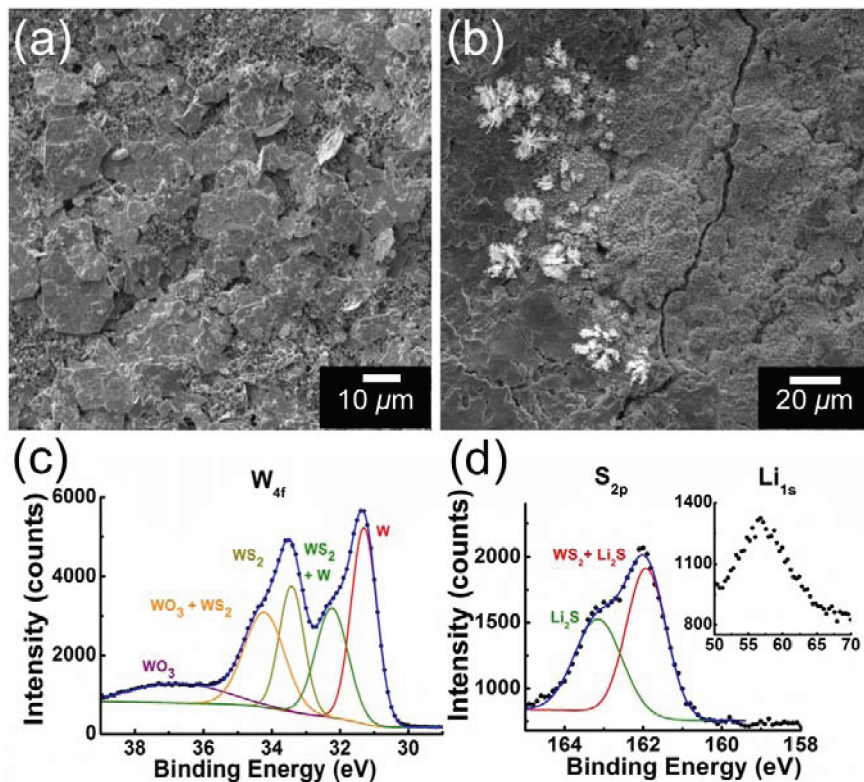


Figure 3. (a,b) SEM micrographs of a superacid-treated WS_2 anode before and after 20 electrochemical cycles, respectively. (c,d) XPS spectra ($\text{W}_{4\text{f}}$ and $\text{S}_{2\text{p}}$, respectively) for the electrochemically cycled WS_2 anode after 20 cycles (dots: measured data; lines: curve fitted data). Inset in panel d is the $\text{Li}_{1\text{s}}$ spectrum.

Table 1. Elemental Composition of Top Surfaces of Superacid-Treated WS_2 Sheets before and after Electrochemical Cycling^a

specimen	elemental composition				empirical formula
	tungsten	lithium	oxygen	sulfur	
anode surface	8.58	N/A	82.4	9.01	WO_{10}S
anode 5 nm sputter	30.64	N/A	20.95	48.4	$\text{WO}_{0.65}\text{S}_{1.6}$
anode after cycling	36.43	30.42	1.88	31.24	$\text{WO}_{0.05}\text{Li}_{0.8}\text{S}_{0.8}$

^aN/A: not available.

The measured galvanometric potential of 2-D WS_2 nanosheets (anode) with respect to Li-metal (cathode) for the first two charge and discharge cycles at a current density of 25 mA/g is plotted in Figure 4a. The cell voltage profiles of lithiation and delithiation cycles are perceived as the electrode's structural evolution and chemical phase transformation at the intended performance rate. At a constant current rate of 25 mA/g and open circuit voltage of approximately 1.5 V, the cell exhibited a first-cycle discharge capacity of 578.6 mAh/g and recovered a full potential of 2.5 V with a reversible capacity of 469.7 mAh/g. A first-cycle loss (ICL) of 18.8% and first-cycle hysteresis of 0.9 V (36% of operating voltage range) were also observed.

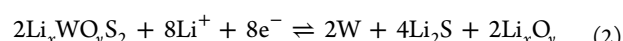
As categorized in Figure 4a, the Li-ion insertion and extraction cycle is observed to exhibit three major phases: phase I as a rapid drop from the open circuit voltage, phase II as a constant voltage plateau, and phase III as a steep voltage drop.

The second phase, which is observed as a plateau (~0.8 V), is known to arise as a result of the reversible conversion reaction

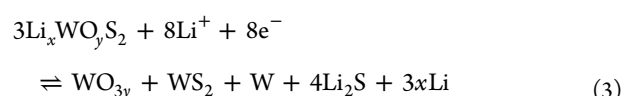
that is typical of binary transition metal compounds. For the given anode, the conversion reaction results in phase transformation of WO_3S_2 ²⁸ summarized in eq 1. The forward reaction (top arrow) corresponds to the discharge (first) half of the electrochemical cycle.



The third phase observed as further insertion of Li-ion at lower voltages could result in decomposition of $\text{Li}_x\text{WO}_3\text{S}_2$ and undergoes a phase change, reducing tungsten (W^{5+} to W^{5-x}) and irreversibly reacting sulfur with lithium as given in eq 2.²⁹



Electrolyte decomposition (reduction) at lower voltages also contributes toward this phase. On the basis of the interpretation of the post-cycling XPS spectra, the intercalation phase could result in multiple entities of WS_2 , WO_3 , and W .



Meanwhile the reversible reaction occurring at the cathode is given as



As each phase during the anode electrochemical cycling corresponds to specific physical processes, comparison of successive cycles can provide useful information regarding the anode's structural changes. On the basis of the dissimilar electrochemical cycling profiles during discharging and

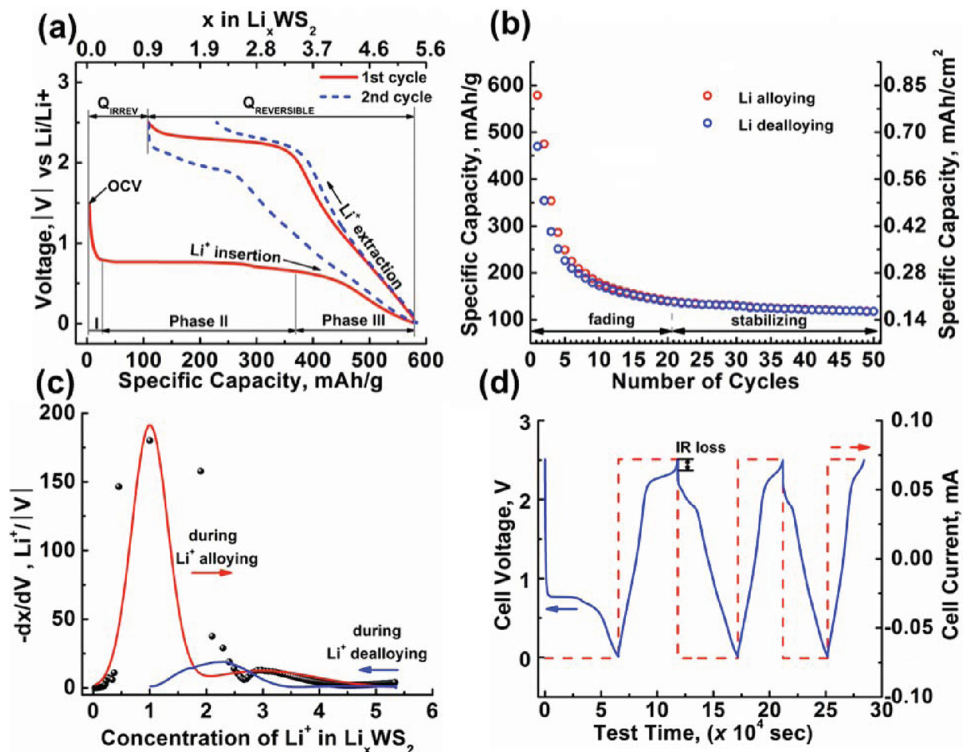


Figure 4. (a) Cell potential corresponding to specific capacity (bottom axis) and moles of Li-ion in the anode (top axis) for the first (solid) and second (dashed) electrochemical lithium insertion and extraction cycles; side reactions of lithium with the electrolyte are ignored in this quantitative analysis. (b) Specific charge and discharge capacities for superacid-functionalized WS₂ specimen measured at 25 mA/g current density starting to stabilize after the 15th cycle. (c) Inverse derivative of Li-ion concentration with respect to the cell potential for the first alloying and dealloying cycles. (d) Cyclic chronopotentiometry waveform for the first three cycles at current density of 25 mA/g.

charging, it can be inferred that the phase transformation is different for each half of the cycle.

As shown in Figure 4a the conversion plateau due to the polarization phenomenon is prominent during the discharge cycle and reduces during the charge half of the cycle, whereas the small phase III (inclined) for the first discharge cycle increases in the first charge and subsequent cycles, suggesting a decrease in capacity contribution due to the conversion reaction and its replacement by the reversible Li-ion intercalation processes.

As seen in Figure 4b, the specific discharge and charge capacities for the cell operated at 25 mA/g drops until the 15th cycle, after which they stabilized. This capacity fading could result from the conversion process of WS₂, structural changes, and volumetric expansion of WS₂ due to Li-ion intercalation, and can lead to loss of connection between conducting particles and current collector. For the cycled WS₂ anode, no evidence of active material being peeled off from the surface was observed, but surface cracks (due to strains induced by structural deformation) were visible under the SEM (Figure 3b). On the other hand, the issue of capacity decay could be attributed to the electrolyte degradation (producing Li₂S_n polysulfide intermediates) during cycling.^{31–33} Hence the issue of depleting capacity with cycling could be addressed by selection of more compatible electrolytes. The further cyclic chronopotentiometry waveform shown in Figure 4d shows a sequentially reducing cycle time for the initial cycles (32.8 h first to 7.4 h for fiftieth cycle), even as the current density is held constant at 25 mA/g. The anode's structural change due to Li-ion intercalation could be the cause of higher alloying rates.²²

Differentiated moles of Li-ion with respect to cell potential, plotted in Figure 4c, qualitatively suggests the rate of ionic mobility at the anode surface and within it. Two distinct peaks (at $x = 1.1$ and 2.9 mols) realized for the Li-ion alloying half of the cycle implies two different rates of alloying with anode material, suggesting ion intercalation as a two-staged process. During the Li-ion dealloying phase, the concentration change follows a similar pattern but in reverse and with lesser intensity, implying a more uniform rate of Li-ion reduction reaction.

Dependence of cell performance on operating current density is demonstrated in Figure 5a. Although the overall capacity remained almost constant, the individual contribution of each phase (described above) changed when operated at variable current densities. Comparison of the critical performance parameters of anodes measured at different current densities is summarized in Table 2. Figure 5b,c,d shows the contribution of each phase in the total capacity for the first, second, and 20th complete cycles at current densities of 50, 25, and 10 mA/g, respectively. Most prominently, the contribution due to conversion reaction and irreversible processes is observed to decrease, while the capacity contribution due to Li-ion intercalation is found to dominate with progressing cycles.

Previously, Julien²² showed that Li-ion intercalation into bulk WS₂ can cause increased conductivity and a reduction in activation energy. Hence, the magnitude of first-cycle alloying and dealloying capacities with low first-cycle loss could be attributed to the ease of Li-ion diffusion in and out of the cleaved WS₂ interlayer spacings. The ICL of about 19% is mainly attributed to the irreversible electrolyte decomposition

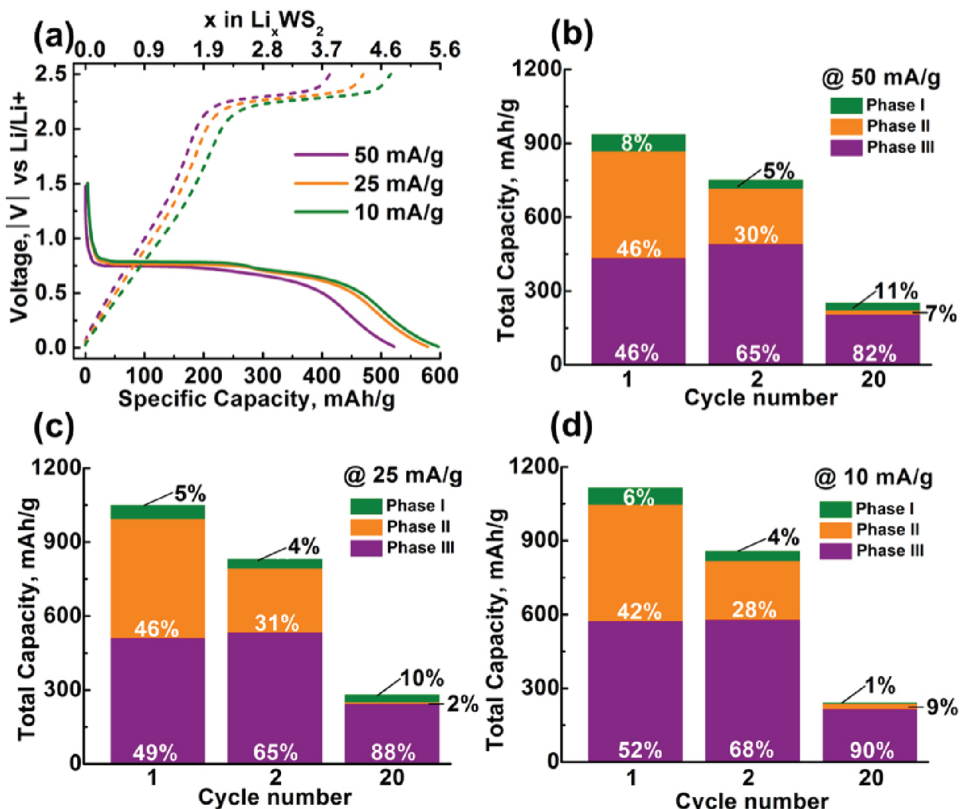


Figure 5. (a) First discharge (solid) and charge (dashed) cycle comparison for the cells operated at specific current densities, and their electrochemical performance in terms of specific capacity (bottom axis) and equivalent moles of Li-ions intercalating in the anode (top axis). Total capacity plot of the characteristic phase distribution for cell operated at (b) 50 mA/g, (c) 25 mA/g, and (d) 10 mA/g.

Table 2. Summary of the Comparative Electrochemical Test Results for WS_2 Anodes^a

WS_2 architecture	lithiation (delithiation) capacity, mAh/g	molar ratio of Li^+/WS_2	first cycle loss, %	hysteresis, volts	current density, mA/g (mA/cm ²)
3R- WS_2 Bulk ref. (23)	64* (58*)	0.6	9	0.6	-0.1
superacid 2H- WS_2	522 (413)	4.8	20.8	1.09	50 (0.06)
superacid 2H- WS_2	579 (470)	5.3	18.8	0.93	25
superacid 2H- WS_2	597 (516)	5.5	13.5	0.96	10

^a* = calculated equivalent specific capacities.

at low voltages (forming a passivating SEI layer) and inactive regions or disconnected phases formed during the first cycle.

The first cycle hysteresis of ~ 0.9 V is the difference of the average potential during Li-ion alloying and dealloying. This hysteresis is conceived to be due to the equilibrium potential difference of dis-similar reactions occurring during alloying and dealloying cycles.³⁴

By comparing the performance of multiple dispersants, we have shown that separation of weakly bonded WS_2 sheets by superacid treatment forms the most stable suspensions at 2 mg/mL. High absorbance in UV-visible (UV-vis) spectroscopy qualitatively supports the highly stable WS_2 concentration in superacid. ζ potential measurements confirm that the superacid-treated WS_2 sheets possess surface charge and electrostatic repulsion between them, thereby forming a stable

suspension. The same approach could also be extended for other TMDCs due to their similar atomic arrangement. XPS analysis of the superacid-treated WS_2 showed W–O type bonds, signifying tungsten oxidation at the edges, while the existence of reduced sulfur phase suggested the acceptance of electrons from the donor superacid species. Thermogravimetric analysis (TGA) of the superacid-treated WS_2 showed a three-staged pattern (similar to the bulk WS_2), except that the weight loss occurred at lower temperatures most likely due to acidic residues and separated single- or few-layer sheets. At higher temperatures, bulk WS_2 showed a continuous weight loss, while acid-treated WS_2 stabilized (possibly due to WO_3 formation). The electrochemical performance of the superacid-treated WS_2 measured in a Li-ion half-cell configuration demonstrated higher first-cycle reversible capacity of 470 mAh/g (equivalent to 5.3Li per WS_2) at a current density of 25 mA/g and voltage hysteresis of 0.93 V. Enhanced capacity is attributed to the increased lithium intercalation between the cleaved superacid-treated WS_2 layers.

EXPERIMENTAL METHODS

Dispersion of WS_2 Sheets. WS_2 powder (2 mg/mL, 99%, Sigma Aldrich) was separately sonicated for 30 min in isopropanol, deionized (DI) water (containing 1.5 mg/mL of NaDDBS), concentrated sulphuric acid, and concentrated chlorosulphonic acid (superacid, 99%, Sigma Aldrich), and the nonexfoliated sheets were allowed to settle. Please note that the superacid was slowly added to the WS_2 powder in an argon-filled glovebox (dew point -50 °C). The solution was then carefully transferred in 1.0 L of distilled water for quenching (done

with extreme caution in a glovebox). Additional dilution with DI water was done to reduce the solution acidity.

Optical absorption spectra in the ultraviolet and visible range were collected on a Cary 500 scan UV-vis near-infrared (NIR) spectrometer by using respective pure solvents as a reference. ζ potential surface measurements were carried out on a ZetaPlus Zeta Potential Analyzer (Brookhaven's Inst. Corp.). The effect of ionic concentration on the potential measured is minimized by using a low concentration of basic (0.01 M NaOH) solution for controlling the pH. SEM images were obtained on a Carl Zeiss EVO low-vacuum SEM. TEM was performed using a Philips CM 100 TEM. The surface chemical composition was studied by X-ray photoelectron spectroscopy (XPS, PHI Quantera SXM) using monochromatic Al K α X-radiation. Electrochemical measurements were accomplished by Battery Test Equipment (Arbin-BT2000) at atmospheric conditions. Thermal stability analysis was carried out on a Shimadzu 50 thermogravimetric analyzer (TGA) up to 1000 °C in flowing air at 20 mL/min.

Battery anodes were prepared by adding superacid-treated WS₂ powder as the active material with acetylene black as the conducting agent and polyvinyl difluoride as the binder in a 8:1:1 ratio, respectively. Approximately 2 g of *N*-methyl pyrrolidone was added as solvent, for obtaining uniform viscosity of the mix. These ingredients were thoroughly mixed with a mortar and pestle until it appeared to be a homogeneous slurry. The slurry was then applied on to a 15 μm -thick copper sheet with 127 μm step applicator blade and then slowly dried at 80 °C for approximately 12 h in an inert atmosphere to vaporize the solvent. Electrodes of 14.3 mm diameter were then punched out for use in the coin cell as a negative electrode.

The gross weight of coated anode material on the copper current collector was measured before the assembly, and the net weight was calculated by subtracting the weight of bare copper. Typical loading of the active material used in each cell was approximately 2.5 mg. For electrochemical testing, 2032 half coin cells were assembled and crimped in an argon glovebox (humidity <15 ppm) with the superacid-treated WS₂ specimen as a negative electrode, while pure lithium metal (14.3 mm diameter, 75 μm thick) acted as the counter electrode. A 25 μm -thick (19 mm diameter) monolayer membrane (Celgard) (soaked in electrolyte for over a fortnight) was used as a separator, and approximately 1 mL electrolyte solution of 1 M LiPF₆ (Alfa Aesar) dissolved in (1:1 v/v) dimethyl carbonate: ethylene carbonate (ionic conductivity 10.7 S/cm) was used as an electrolyte. Thereafter, the assembled batteries were tested for electrochemical performance in the voltage range of 10 mV to 2.5 V with constant current densities of 10, 25, and 50 mA/g during both discharge and charge half cycles in atmospheric conditions.

AUTHOR INFORMATION

Corresponding Author

*E-mail: gurpreet@ksu.edu; Tel.: +1-785-532-7085; Fax: +1-785-532-7057.

Notes

The authors declare no competing financial interest.

ACKNOWLEDGMENTS

G.S. would like to acknowledge financial support from Kansas State University. The authors would like to thank Professor Rishi Raj (University of Colorado at Boulder) for providing

access to the high-precision glovebox for cell assembly, Dr. John Desper, Dr. Stefan Bossmann, and Dr. Hongwang Wang (all Kansas State University) for ζ -potential measurements, and Dr. Jerry Hunter (Virginia Tech) for XPS.

REFERENCES

- Zhao, H. Y.; Oyama, S. T.; Naeemi, E. D. Hydrogen Storage Using Heterocyclic Compounds: The Hydrogenation of 2-Methylthiophene. *Catal. Today* **2010**, *149*, 172–184.
- Radisavljevic, B.; Radenovic, A.; Brivio, J.; Giacometti, V.; Kis, A. Single-Layer MoS₂ Transistors. *Nat. Nanotechnol.* **2011**, *6*, 147–150.
- Polcar, T.; Nossa, A.; Evaristo, M.; Cavaleiro, A. Nanocomposite Coatings of Carbon-Based and Transition Metal Dichalcogenides Phases. *Rev. Adv. Mater. Sci.* **2007**, *15*, 118–126.
- Feng, C.; Huang, L.; Guo, Z.; Liu, H. Synthesis of Tungsten Disulfide (WS₂) Nanoflakes for Lithium Ion Battery Application. *Electrochim. Commun.* **2007**, *9*, 119–122.
- Frey, G. L.; Reynolds, K. J.; Friend, R. H.; Cohen, H.; Feldman, Y. Alkali Metal Intercalated Fullerene-Like MS₂ (M = W, Mo) Nanoparticles and Their Properties. *J. Am. Chem. Soc.* **2003**, *125*, 5998–6007.
- Makovicky, E. Crystal Structures of Sulfides and Other Chalcogenides. *Rev. Mineral. Geochem.* **2006**, *61*, 7–125.
- Wilson, J. A.; Yoffe, A. D. Transition Metal Dichalcogenides Discussion and Interpretation of Observed Optical, Electrical and Structural Properties. *Adv. Phys.* **1969**, *18*, 193–335.
- Ramasubramaniam, A.; Naveh, D.; Towe, E. Tunable Band Gaps in Bilayer Transition-Metal Dichalcogenides. *Phys. Rev. B* **2011**, *84*, 205325.
- Seo, J.; Jun, Y.; Park, S.; Nah, H.; Moon, T.; Park, B.; Kim, J.; Kim, Y. J.; Cheon, J. Two-Dimensional Nanosheet Crystals. *Angew. Chem., Int. Ed.* **2007**, *46*, 8828–8831.
- Wu, Z.; Wang, D.; Zan, X.; Sun, A. Synthesis of WS₂ Nanosheets by a Novel Mechanical Activation Method. *Mater. Lett.* **2010**, *64*, 856–858.
- Matte, H. S. S. R.; Gomathi, A.; Manna, A. K.; Late, D. J.; Datta, R.; Pati, S. K.; Rao, C. N. R. MoS₂ and WS₂ Analogues of Graphene. *Angew. Chem., Int. Ed.* **2010**, *49*, 4059–4062.
- Coleman, J. N.; Lotya, M.; O'Neill, A.; Bergin, S. D.; King, P. J.; Khan, U.; Young, K.; Gaucher, A.; De, S.; Smith, R. J.; et al. Two-Dimensional Nanosheets Produced by Liquid Exfoliation of Layered Materials. *Science* **2011**, *331*, 568–571.
- Kamat, P. V. Graphene-Based Nanoassemblies for Energy Conversion. *J. Phys. Chem. Lett.* **2011**, *2*, 242–251.
- Schniepp, H. C.; Li, J. L.; McAllister, M. J.; Sai, H.; Herrera-Alonso, M.; Adamson, D. H.; Prud'homme, R. K.; Car, R.; Saville, D. A.; Aksay, I. A. Functionalized Single Graphene Sheets Derived from Splitting Graphite Oxide. *J. Phys. Chem. B* **2006**, *110*, 8535–8539.
- Green, A. A.; Hersam, M. C. Emerging Methods for Producing Monodisperse Graphene Dispersion. *J. Phys. Chem. Lett.* **2010**, *1*, 544–549.
- Behabtu, N.; Lameda, J. R.; Green, M. J.; Higginbotham, A. L.; Sinitskii, A.; Kosynkin, D. V.; Tsentalovich, D.; Parra-Vasquez, A. N. G.; Schmidt, J.; Kesselman, E.; et al. Spontaneous High-Concentration Dispersions and Liquid Crystals of Graphene. *Nat. Nanotechnol.* **2010**, *5*, 406–411.
- Davis, V. A.; Parra-Vasquez, A. N. G.; Green, M. J.; Rai, P. K.; Behabtu, N.; Prieto, V.; Booker, R. D.; Schmidt, J.; Kesselman, E.; Zhou, W.; et al. True Solutions of Single-Walled Carbon Nanotubes for Assembly Into Macroscopic Materials. *Nat. Nanotechnol.* **2009**, *4*, 830–834.
- Cremlyn, R. J. *Chlorosulfonic Acid: A Versatile Reagent*; Royal Society of Chemistry: London, 2002.
- Wang, G. X.; Bewlay, S.; Yao, J.; Liu, H. K.; Dou, S. X. Tungsten Disulfide Nanotubes for Lithium Storage. *Electrochim. Solid State* **2004**, *7*, A321–A323.
- Wang, S.; Li, G.; Du, G.; Li, L.; Jiang, X.; Feng, C.; Guo, Z.; Kim, S. Synthesis and Characterization of Cobalt-Doped WS₂

- Nanorods for Lithium Battery Applications. *Nanoscale Res. Lett.* **2010**, *5*, 1301–1306.
- (21) Yoon, S.; Jo, C.; Noh, S. Y.; Lee, C. W.; Song, J. H.; Lee, J. Development of a High-Performance Anode for Lithium Ion Batteries Using Novel Ordered Mesoporous Tungsten Oxide Materials with High Electrical Conductivity. *Phys. Chem. Chem. Phys.* **2011**, *13*, 11060–11066.
- (22) Julien, C. M. Charge Transfer and Related Properties. *Mater. Sci. Eng., R* **2003**, *40*, 47–102.
- (23) Yebka, B.; Julien, C. Studies of Lithium Intercalation in 3R-WS₂. *Solid State Ionics* **1996**, *90*, 141–149.
- (24) Du, G.; Guo, Z.; Wang, S.; Zeng, R.; Chen, Z.; Liu, H. Superior Stability and High Capacity of Restacked Molybdenum Disulfide as Anode Material for Lithium Ion Batteries. *Chem. Commun.* **2010**, *46*, 1106–1108.
- (25) Lotya, M.; Hernandez, Y.; King, P. J.; Smith, R. J.; Nicolosi, V.; Karlsson, L. S.; Blighe, F. M.; De, S.; Wang, Z.; McGovern, I. T.; et al. Liquid Phase Production of Graphene by Exfoliation of Graphite in Surfactant/Water Solutions. *J. Am. Chem. Soc.* **2009**, *131*, 3611–3620.
- (26) Stankovich, S.; Dikin, D. A.; Pineri, R. D.; Kohlhaas, K. A.; Kleinhammes, A.; Jia, Y.; Wu, Y.; Nguyen, S. T.; Ruoff, R. S. Synthesis of Graphene-Based Nanosheets via Chemical Reduction of Exfoliated Graphite Oxide. *Carbon* **2007**, *45*, 1558–1565.
- (27) Li, Y.; Zhao, Y. M.; Ma, R. Z.; Zhu, Y. Q.; Fisher, N.; Jin, Y. Z.; Zhang, X. P. Novel Route to Wox Nanorods and WS₂ Nanotubes from WS₂ Inorganic Fullerenes. *J. Phys. Chem. B* **2006**, *110*, 18191–18195.
- (28) Martin-Litas, I.; Vinatier, P.; Levasseur, A.; Dupin, J. C. Characterisation of R.F. Sputtered Tungsten Disulfide and Oxsulfide Thin Films. *Thin Solid Films* **2002**, *416*, 1–9.
- (29) Ho, S. F.; Contarini, S.; Rabalais, J. W. Ion-Beam-Induced Chemical-Changes in the Oxyanions and Oxides. *J. Phys. Chem.* **1987**, *91*, 4779–4788.
- (30) Selwyn, L. S.; Mckinnon, W. R.; Vonsacken, U.; Jones, C. A. Lithium Electrochemical-Cells at Low-Voltage - Decomposition of Mo and W Dichalcogenides. *Solid State Ionics* **1987**, *22*, 337–344.
- (31) Contarini, S.; Rabalais, J. W. Ion Bombardment-Induced Decomposition of Li and Ba Sulfates and Carbonates Studied by X-ray Photoelectron-Spectroscopy. *J. Electron Spectrosc.* **1985**, *35*, 191–201.
- (32) Yamin, H.; Peled, E. Electrochemistry of a Nonaqueous Lithium/Sulfur Cell. *J. Power Sources* **1983**, *9*, 281–287.
- (33) Ryu, H. S.; Guo, Z.; Ahn, H. J.; Cho, G. B.; Liu, H. Investigation of Discharge Reaction Mechanism of Lithium Liquid Electrolyte Sulfur Battery. *J. Power Sources* **2009**, *189*, 1179–1183.
- (34) Cabana, J.; Monconduit, L.; Larcher, D.; Rosa Palacin, M. Beyond Intercalation-Based Li-Ion Batteries: The State of the Art and Challenges of Electrode Materials Reacting Through Conversion Reactions. *Adv. Mater.* **2010**, *22*, E170–E192.